

Cite this: *J. Mater. Chem. A*, 2020, **8**, 13776

High-energy O3-Na_{1-2x}Ca_x[Ni_{0.5}Mn_{0.5}]O₂ cathodes for long-life sodium-ion batteries†

Tae-Yeon Yu,^a Jongsoon Kim,^b Jang-Yeon Hwang,^c Hyungsub Kim,^d Geumjae Han,^a Hun-Gi Jung^{b,e} and Yang-Kook Sun^{b,*a}

To facilitate the practical realization of sodium-ion batteries, the energy density, determined by the output operating voltage and/or capacity, needs to be improved to the level of commercial Li-ion batteries. Herein, O3-type Na_{0.98}Ca_{0.01}[Ni_{0.5}Mn_{0.5}]O₂ is synthesized by incorporating Ca²⁺ into the NaO₆ octahedron of Na[Ni_{0.5}Mn_{0.5}]O₂ and its potential use as a cathode material for high energy density SIBs is demonstrated. The ionic radius of calcium (≈1.00 Å) is similar to that of sodium (≈1.02 Å); hence, it is energetically favorable for calcium to occupy sites in the sodium layers. Within a wide operating voltage range of 2.0–4.3 V, O3-type Na_{0.98}Ca_{0.01}[Ni_{0.5}Mn_{0.5}]O₂ exhibits a reversible O3–P3–O3 phase transition with small volume changes compared to Ca-free Na[Ni_{0.5}Mn_{0.5}]O₂ because of the strong interaction between Ca²⁺ and O²⁻ and delivers a high reversible capacity of 209 mA h g⁻¹ at 15 mA g⁻¹ with improved cycling stability. Moreover, Ca substitution improves the practically useful aspects such as thermal and air stability. A prototype pouch full cell with a hard carbon anode shows an excellent capacity retention of 67% over 300 cycles. Thus, this study provides an efficient and simple method to boost the performance and applicability of layered oxide cathode materials for practical applications.

Received 11th May 2020
Accepted 21st June 2020

DOI: 10.1039/d0ta04847j

rsc.li/materials-a

Introduction

Energy storage is the key for the application of renewable technologies and will enable the energy to be used as per the consumer's convenience, time, and space. Among the various technologies, the battery plays a key role in the successful use of extra energy and/or renewable energy; particularly, advances in lithium-ion batteries (LIBs) have significantly improved the quality of life around the globe since their commercialization by Sony Corporation in the 1990s.¹ To date, the global LIB market has seen massive growth, with a focus on electric vehicles along with IT devices. However, the increasing lithium scarcity will increase the price. This will lead to a sharp rise in the production cost of LIBs.^{2,3} Hence, a revolutionary paradigm is required to design next-generation energy storage systems at a low cost with higher energy, higher power, longer lifetime, and superior

safety than LIBs. Sodium-ion batteries (SIBs), which operate under a “rocking-chair” Na storage mechanism similar to that of Li in LIBs, have emerged as a potential alternative to LIBs considering the abundance of Na resources.^{4–6} The energy density of SIBs, in a similar manner to LIBs, is mainly determined collectively by the specific capacity and working voltage of the cathode materials. Hence, tremendous efforts have been devoted to exploring and developing cathode materials. Among the various candidates, O3-type layered oxide materials are very fascinating because they have the same crystal structure as commercial LiCoO₂, thereby exhibiting good practical applicability.^{7–10}

In 2012, Komaba *et al.* presented the findings of research on Co-free O3-Na[Ni_{0.5}Mn_{0.5}]O₂, in which the average oxidation states of Ni and Mn are 2+ and 4+, respectively.¹¹ To date, O3-Na[Ni_{0.5}Mn_{0.5}]O₂ has been considered as one of the most promising cathode materials because of its high capacity and good practical applicability;^{12–15} however, O3-Na[Ni_{0.5}Mn_{0.5}]O₂ typically has a lower working potential than its lithium-ion counterpart (≈3.7 V *vs.* Li/Li⁺ for O3-Li[Ni_{0.5}Mn_{0.5}]O₂; 3.0 V *vs.* Na/Na⁺ for O3-Na[Ni_{0.5}Mn_{0.5}]O₂) due to the larger ionic size and lower Lewis acidity of Na⁺ than Li⁺.¹⁴ Such a low operating voltage greatly lowers the energy density of SIBs. Hence, an effective approach would be to elevate the operating voltage of the battery, which requires the use of O3-Na[Ni_{0.5}Mn_{0.5}]O₂ with high voltage *versus* Na/Na⁺. However, O3-Na[Ni_{0.5}Mn_{0.5}]O₂ generally experiences an undesirable surface reaction with electrolyte solution and inevitable irreversible phase transition

^aDepartment of Energy Engineering, Hanyang University, Seoul 04763, Republic of Korea. E-mail: yksun@hanyang.ac.kr

^bDepartment of Nanotechnology and Advanced Materials Engineering, Sejong University, Seoul 05006, Republic of Korea

^cDepartment of Materials Science and Engineering, Chonnam National University, Gwangju 61186, Republic of Korea

^dKorea Atomic Energy Research Institute, Daejeon 34507, Republic of Korea

^eCenter for Energy Storage Research, Green City Technology Institute, Korea Institute of Science and Technology, Seoul 02792, South Korea

† Electronic supplementary information (ESI) available: SEM images; results of Rietveld refinements; TEM images; additional electrochemical test results; XANES data; *ex situ* XRD results. See DOI: 10.1039/d0ta04847j

occurs *via* the redox reaction of $\text{Ni}^{2+}/\text{Ni}^{4+}$, which affects the cycling stability within the high-voltage window.¹⁵ Especially, high extraction of Na^+ leads to interlayer gliding with destruction of the structure, which immediately causes poor cycling performance.¹⁶ Nevertheless, innovative studies on O3-Na $[\text{Ni}_{0.5}\text{Mn}_{0.5}]\text{O}_2$, including cationic substitution and doping into transition metal layers or surface coating, have been investigated as efficient strategies to enhance the high voltage stability by avoiding the above high voltage phase transition.^{16–22} However, although these results appear impressive, they exhibit insufficient capacities which are well below those viable for commercial LIB applications.

Herein, we demonstrate that an unprecedented high capacity, cycling stability, and power capability can be attained using an O3- $\text{Na}_{0.98}\text{Ca}_{0.01}[\text{Ni}_{0.5}\text{Mn}_{0.5}]\text{O}_2$ cathode within a wide operating voltage window of 2.0–4.3 V (*vs.* Na/Na^+). It is known that calcium (Ca) is one of the most abundant elements in the Earth, which indicates that the Ca-based-substitution has the advantage of low production cost compared to other metal-based-substitutions. Moreover, most calcium-based compounds, such as calcium hydroxide ($\text{Ca}(\text{OH})_2$), are non-toxic; thus, it is easy to prepare calcium-substituted electrode materials through simple synthesis methods. Without disrupting the O3 phase structure, Ca^{2+} ions were incorporated into bulk Na ion sites; the ionic species were inserted in an octahedral (O) environment because Ca^{2+} is electrostatically stable in the edge-sharing MO_6 octahedral layer.^{23,24} Owing to the strong interaction between Ca^{2+} and O^{2-} , the presence of Ca^{2+}

ions in the crystal structure significantly mitigated the volume expansion when extracting maximum Na ions from O3- $\text{Na}_{0.98}\text{Ca}_{0.01}[\text{Ni}_{0.5}\text{Mn}_{0.5}]\text{O}_2$, resulting in structural stability and improved cyclability. Within a wide operating voltage range of 2.0–4.3 V, O3- $\text{Na}_{0.98}\text{Ca}_{0.01}[\text{Ni}_{0.5}\text{Mn}_{0.5}]\text{O}_2$ exhibits reversible O3–P3–O3 phase transition with smaller volume changes compared to those of Ca-free $\text{Na}[\text{Ni}_{0.5}\text{Mn}_{0.5}]\text{O}_2$. In addition, O3- $\text{Na}_{0.98}\text{Ca}_{0.01}[\text{Ni}_{0.5}\text{Mn}_{0.5}]\text{O}_2$ displays an unprecedented high specific capacity of 209 mA h g^{-1} at 15 mA g^{-1} and outstanding cycling stability and rate capability with 58% capacity retention at 10C. In a prototype pouch full cell using a hard carbon anode, the O3- $\text{Na}_{0.98}\text{Ca}_{0.01}[\text{Ni}_{0.5}\text{Mn}_{0.5}]\text{O}_2$ cathode delivered excellent capacity retention of 67% after 300 cycles, highlighting its promising potential as a cathode material for practical SIBs. The overall reaction mechanism of O3-Na $[\text{Ni}_{0.5}\text{Mn}_{0.5}]\text{O}_2$ was clearly identified through a combination of first-principles calculations with experiments such as *ex situ* X-ray absorption near edge structure and *operando* synchrotron X-ray diffraction.

Results and discussion

Synthesis and characterization

The $[\text{Ni}_{0.5}\text{Mn}_{0.5}](\text{OH})_2$ precursor was initially synthesized *via* a typical co-precipitation method.¹⁹ Scanning electron microscope (SEM) images of the products indicated the presence of spherical secondary particles with an average diameter of $7 \mu\text{m}$ (Fig. 1a and S1a†). The spherical shape of the thermally sodiated $\text{Na}[\text{Ni}_{0.5}\text{Mn}_{0.5}]\text{O}_2$ and Ca-substituted

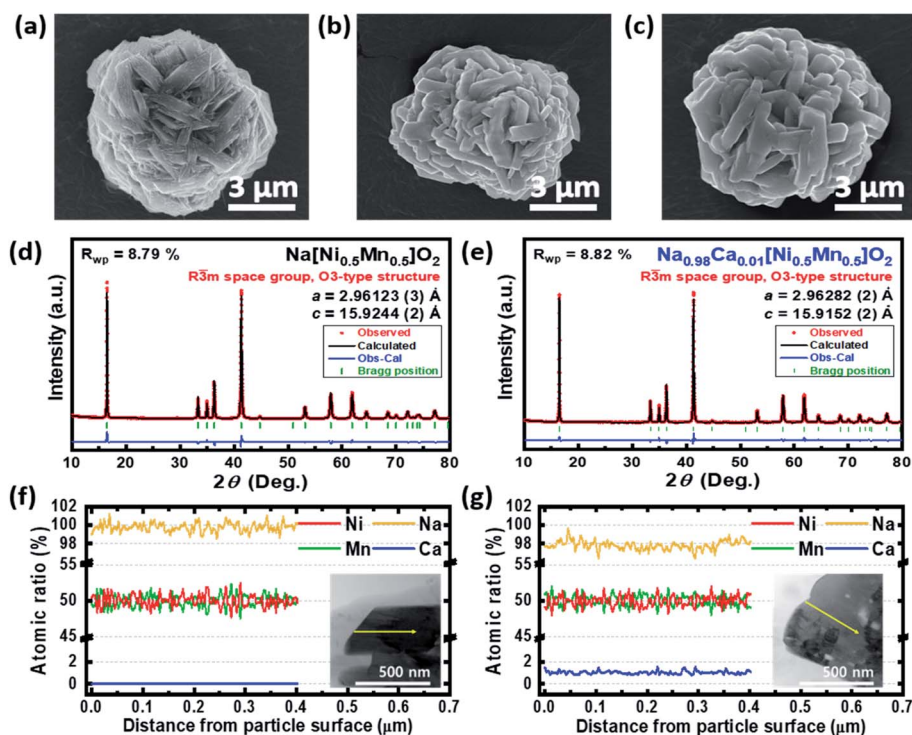


Fig. 1 SEM images of (a) the $[\text{Ni}_{0.5}\text{Mn}_{0.5}](\text{OH})_2$ precursor, (b) $\text{Na}[\text{Ni}_{0.5}\text{Mn}_{0.5}]\text{O}_2$, and (c) Ca-substituted $\text{Na}_{0.98}\text{Ca}_{0.01}[\text{Ni}_{0.5}\text{Mn}_{0.5}]\text{O}_2$ cathodes. Profile-matched XRD patterns of (d) $\text{Na}[\text{Ni}_{0.5}\text{Mn}_{0.5}]\text{O}_2$ and (e) Ca-substituted $\text{Na}_{0.98}\text{Ca}_{0.01}[\text{Ni}_{0.5}\text{Mn}_{0.5}]\text{O}_2$ cathodes calculated using the Rietveld refinement method. TEM-EDX line scanning results of (f) $\text{Na}[\text{Ni}_{0.5}\text{Mn}_{0.5}]\text{O}_2$ and (g) $\text{Na}_{0.98}\text{Ca}_{0.01}[\text{Ni}_{0.5}\text{Mn}_{0.5}]\text{O}_2$ cathodes.

$\text{Na}_{0.98}\text{Ca}_{0.01}[\text{Ni}_{0.5}\text{Mn}_{0.5}]\text{O}_2$ particles in Fig. 1b and c (and also Fig. S1b and c†) was well preserved, and the average particle diameter was nearly the same as that of the hydroxide precursor after high-temperature calcination at 800 °C. Regardless of the presence/absence of Ca substitution, the calcined products exhibited a smooth particle surface without the formation of impurities, indicating that Na^+ and Ca^{2+} ions may be incorporated into the crystal structure. The chemical composition of $\text{Na}[\text{Ni}_{0.5}\text{Mn}_{0.5}]\text{O}_2$ and $\text{Na}_{0.98}\text{Ca}_{0.01}[\text{Ni}_{0.5}\text{Mn}_{0.5}]\text{O}_2$ was confirmed by inductively coupled plasma (ICP)-optical emission spectrometry (OES) analysis (see the Table S1†). To obtain structural information on both products, synchrotron powder X-ray diffraction (XRD) was conducted. The XRD patterns of both $\text{Na}[\text{Ni}_{0.5}\text{Mn}_{0.5}]\text{O}_2$ and $\text{Na}_{0.98}\text{Ca}_{0.01}[\text{Ni}_{0.5}\text{Mn}_{0.5}]\text{O}_2$ revealed an O3-type layered structure (isostructural with $\alpha\text{-NaFeO}_2$, belonging to the $R\bar{3}m$ space group), as shown in Fig. 1d and e. The refined XRD patterns revealed a good agreement between the observed and simulated data for the synthesized materials. Detailed structural information such as substitution of Ca^{2+} for Na^+ in the structure is provided in Tables S2 and S3.† It is known that the ionic radius of Ca^{2+} (≈ 1.00 Å) is very similar to that of Na^+ (≈ 1.02 Å) but different from those of Ni^{2+} (≈ 0.69 Å) and Mn^{4+} (≈ 0.53 Å), which implies that Ca^{2+} ions are preferentially substituted for Na^+ ions rather than Ni^{2+} or Mn^{4+} .²⁵ If numerous Ca^{2+} ions are substituted into the O3- $\text{Na}[\text{Ni}_{0.5}\text{Mn}_{0.5}]\text{O}_2$ structure, a few Ca^{2+} ions can be substituted for Ni^{2+} ions because of structural instability resulting from the existence of too many Ca^{2+} ions in Na layers in the structure. In case of our research, however, the amount of substituted Ca^{2+} ions in the O3- $\text{Na}[\text{Ni}_{0.5}\text{Mn}_{0.5}]\text{O}_2$ structure is just 0.01 mol, which implies that a negligible amount of Ca^{2+} ions is substituted for Ni^{2+} or Mn^{4+} ions. In particular, we verified through Rietveld refinement that the c -lattice parameters of O3- $\text{Na}[\text{Ni}_{0.5}\text{Mn}_{0.5}]\text{O}_2$ decreased from 15.9244 Å to 15.9152 Å upon substitution of 0.01 mol of Ca^{2+} ions into the structure. If Ca^{2+} ions are substituted not for Na^+ ions but for Ni^{2+} ions, it is probable that the c -lattice parameter will increase because of the larger ionic radius of Ca^{2+} (≈ 1.00 Å) than that of Ni^{2+} (≈ 0.69 Å). Thus, the decreased c -lattice parameter results from the strengthened $\text{O}^{2-}\text{-Ca}^{2+}\text{-O}^{2-}$ bonding compared to $\text{O}^{2-}\text{-Na}^+\text{-O}^{2-}$ in the layered-type crystal structure, which indicates the substitution of Na^+ ions for Ca^{2+} ions in O3- $\text{Na}[\text{Ni}_{0.5}\text{Mn}_{0.5}]\text{O}_2$. In addition, it was verified that the crystal structure of O3- $\text{Na}[\text{Ni}_{0.5}\text{Mn}_{0.5}]\text{O}_2$ is well retained without formation of any impurities or Ca-related phases despite addition of 0.01 mol of Ca^{2+} ions and deficiency of 0.02 mol of Na^+ ions (Fig. S2†). Furthermore, we compared the (003) peak between pristine O3- $\text{Na}[\text{Ni}_{0.5}\text{Mn}_{0.5}]\text{O}_2$ and O3- $\text{Na}_{0.98}\text{Ca}_{0.01}[\text{Ni}_{0.5}\text{Mn}_{0.5}]\text{O}_2$ (Fig. S3†). It was verified that the (003) peak of O3- $\text{Na}_{0.98}\text{Ca}_{0.01}[\text{Ni}_{0.5}\text{Mn}_{0.5}]\text{O}_2$ is observed at higher 2θ angle than that of pristine O3- $\text{Na}[\text{Ni}_{0.5}\text{Mn}_{0.5}]\text{O}_2$, which indicates a decrease of the c -lattice parameter upon substitution of 0.01 mol of Ca^{2+} ions. Moreover, Fig. S4† shows that there is no coating layer on the surface of not only pristine O3- $\text{Na}[\text{Ni}_{0.5}\text{Mn}_{0.5}]\text{O}_2$ but also O3- $\text{Na}_{0.98}\text{Ca}_{0.01}[\text{Ni}_{0.5}\text{Mn}_{0.5}]\text{O}_2$ particles, and the particle sizes of pristine O3- $\text{Na}[\text{Ni}_{0.5}\text{Mn}_{0.5}]\text{O}_2$ and O3- $\text{Na}_{0.98}\text{Ca}_{0.01}[\text{Ni}_{0.5}\text{Mn}_{0.5}]\text{O}_2$ are similar to each other. The absence of a coating layer on the surface of O3- $\text{Na}_{0.98}\text{Ca}_{0.01}[\text{Ni}_{0.5}\text{Mn}_{0.5}]\text{O}_2$ particles is also

confirmed through analysis using transmission electron microscopy-energy dispersive X-ray spectroscopy (TEM-EDX) elementary line scanning (Fig. 1f and g). Moreover, Ca substitution had no effect on the final distribution of transition metals. Both Ni and Mn were homogeneously distributed throughout the particle depth, showing constant concentrations of 50 at% each. However, the concentration of Na decreased to 98 at% throughout the particle, while 1 at% Ca was uniformly incorporated into the particle structure. Meanwhile, even when the substitution level of Ca^{2+} ions into Na sites was further increased to 0.02 and 0.03 mol, $\text{Na}_{0.96}\text{Ca}_{0.02}[\text{Ni}_{0.5}\text{Mn}_{0.5}]\text{O}_2$ and $\text{Na}_{0.94}\text{Ca}_{0.03}[\text{Ni}_{0.5}\text{Mn}_{0.5}]\text{O}_2$ maintained the original O3-type crystal structure but revealed a minor impurity phase (Ca_2MnO_4) due to the limit of Ca solubility in $\text{Na}[\text{Ni}_{0.5}\text{Mn}_{0.5}]\text{O}_2$ (Fig. S2†). Moreover, the deviation of Na confirmed by the ICP result increased with increasing Ca substitution levels for both cathode materials; this is probably due to a decrease of Na with increasing Ca substitution levels, and volatilization of Na during the calcination process despite the presence of 5% excess sodium carbonate. By combining the aforementioned ICP, TEM-EDX, and XRD results, we can conclude that 0.01 mol of Ca was successfully substituted into bulk Na sites by forming $\text{Na}_{0.98}\text{Ca}_{0.01}[\text{Ni}_{0.5}\text{Mn}_{0.5}]\text{O}_2$ without structural changes or an impurity phase.

Electrochemical properties

The fundamental electrochemical sodium storage performances of the $\text{Na}_{1-2x}\text{Ca}_x[\text{Ni}_{0.5}\text{Mn}_{0.5}]\text{O}_2$ ($x = 0, 0.01, 0.02$ and 0.03) cathodes were analysed within a wide operating voltage range of 2.0–4.3 V and the results are shown in Fig. 2. Regardless of the level of Ca substitution, for all samples, the first charge–discharge curves (Fig. 2a) involved several voltage plateaus and steps, which clearly reflect the typical multi-stage phase transition. Upon charging above 4.0 V (highly de-sodiated level), the small amount of Na^+ could not sufficiently screen the interlayer O–O repulsive interaction;^{26,27} hence, a long plateau was observed along with MeO_2 slab gliding to minimize the energy. This long plateau also represents the extent of volume changes in the O3-type cathode structure caused by the transformation of the hexagonal P3 phase into the hexagonal O3′–hexagonal O3′ mixed phase.²² During discharge, the reversible capacities obtained from the $\text{Na}_{1-2x}\text{Ca}_x[\text{Ni}_{0.5}\text{Mn}_{0.5}]\text{O}_2$ cathodes were 212, 209, 204, and 198 mA h g^{-1} for $x = 0, 0.01, 0.02,$ and 0.03 , respectively. With increasing substitution level of Ca into Na sites, the reversible capacity of the $\text{Na}_{1-2x}\text{Ca}_x[\text{Ni}_{0.5}\text{Mn}_{0.5}]\text{O}_2$ cathodes tended to decrease, which is directly related to the substitution of electrochemically inactive Ca^{2+} ions. Surprisingly, the Ca-substituted cathodes showed a remarkable improvement in the cycling performance and rate capability within the wide voltage window. The cycling performances of the $\text{Na}_{1-2x}\text{Ca}_x[\text{Ni}_{0.5}\text{Mn}_{0.5}]\text{O}_2$ ($x = 0, 0.01, 0.02$ and 0.03) cathodes at a current density of 75 mA g^{-1} were compared, as shown in Fig. 2b. Notably, the $\text{Na}_{0.98}\text{Ca}_{0.01}[\text{Ni}_{0.5}\text{Mn}_{0.5}]\text{O}_2$ cathode exhibited the highest capacity of 198 mA h g^{-1} at the first cycle and an optimal cycling stability with $\approx 75\%$ of the reversible capacity retained after 100 cycles. In contrast, $\text{Na}[\text{Ni}_{0.5}\text{Mn}_{0.5}]\text{O}_2$

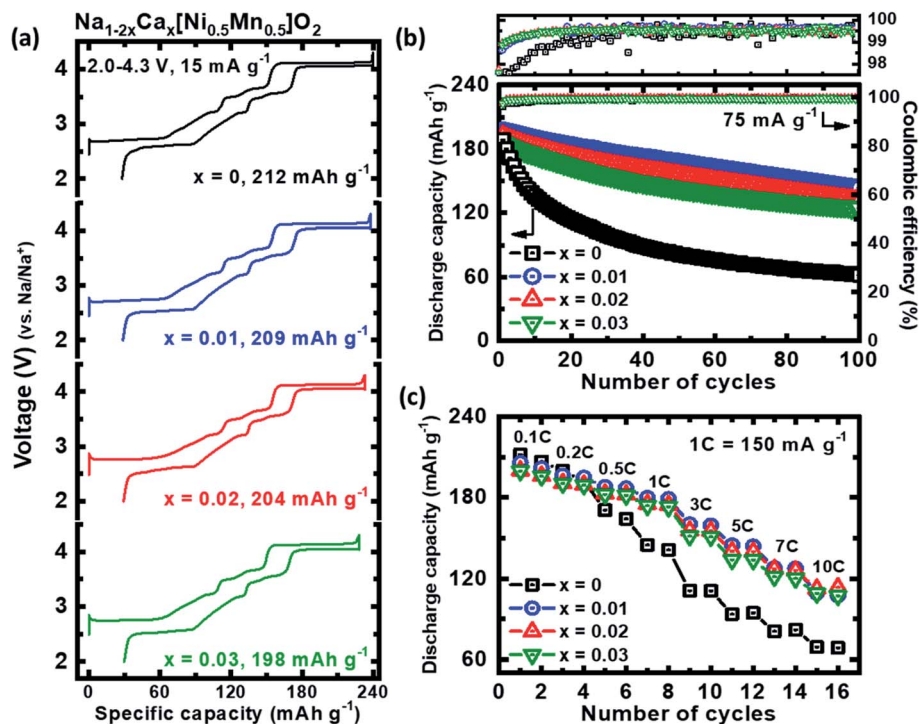


Fig. 2 Electrochemical performances of Na_{1-2x}Ca_x[Ni_{0.5}Mn_{0.5}]O₂ ($x = 0-0.03$) cathodes. (a) Charge–discharge profiles at a current density of 15 mA g⁻¹. (b) Cycling stability using a coin-type cell at 75 mA g⁻¹ at 30 °C (upper figure: enlarged graph of coulombic efficiency vs. number of cycles). (c) Rate capability at various current densities from 15 mA g⁻¹ to 1500 mA g⁻¹ in the voltage range of 2.0–4.3 V.

exhibited fast capacity fading from 189 mA h g⁻¹ at the first cycle to 62 mA h g⁻¹ after 100 cycles, corresponding to a capacity retention of only 33%. Meanwhile, the dQ/dV profiles of the cathodes showed all phase transitions relevant to the O3–P3–O3 phase during cycling (Fig. S5†). It should be noted that the peak intensity and the position for each cathode material in the dQ/dV profiles reflect the level of reversibility of the redox processes. As cycling proceeded, all redox peaks for the Ca-substituted Na_{0.98}Ca_{0.01}[Ni_{0.5}Mn_{0.5}]O₂ cathode were very stably maintained, showing a reversible series of Na⁺ ion extraction/insertion processes. However, all oxidation and reduction peaks for the Na[Ni_{0.5}Mn_{0.5}]O₂ cathode remarkably disappeared after only the 50th cycle. The effect of Ca substitution on the power capability of Na_{1-2x}Ca_x[Ni_{0.5}Mn_{0.5}]O₂ ($x = 0, 0.01, 0.02$, and 0.03) cathodes was also investigated for their possible high-power applications (Fig. 2c). For all current rates from 0.1C (15 mA g⁻¹) to 10C (1500 mA g⁻¹), the Ca substituted cathodes showed a significant improvement in capacity retention; in particular, the Na_{0.98}Ca_{0.01}[Ni_{0.5}Mn_{0.5}]O₂ cathode could deliver 53% of its initial capacity at 10C, while the Na[Ni_{0.5}Mn_{0.5}]O₂ cathode approached only 60 mA h g⁻¹. Furthermore, we tested the electrochemical performance of small amount of Ca-substituted cathodes under the same conditions to verify the optimal level of Ca-substitution in the O3–Na[Ni_{0.5}Mn_{0.5}]O₂ cathode (Fig. S6†). As expected, the discharge capacities tended to decrease with increasing substitution amount of Ca. Moreover, the Ca-substituted cathodes demonstrated stabilized capacity retention, and the retention was improved with increasing amount of Ca substitution from 0.005 to 0.01 mol in

Na sites. From this result, we infer that the presence of Ca²⁺ ions in Na sites stabilized the crystal structure when extracting maximum Na ions but Ca substitution amounts below 0.01 mol are insufficient to exhaustively stabilize the crystal structure. Consequently, the Na_{0.98}Ca_{0.01}[Ni_{0.5}Mn_{0.5}]O₂ in this study manifested optimum sodium storage behaviour for high performance SIBs.

Investigation of structural evolution

To investigate the electrochemical Na ion storage mechanism on the Na[Ni_{0.5}Mn_{0.5}]O₂ and Na_{0.98}Ca_{0.01}[Ni_{0.5}Mn_{0.5}]O₂ cathodes upon Na ion extraction/insertion, cyclic voltammetry was performed (Fig. S7†). Both cathodes underwent a series of phase transitions (O3_{hex.} → O'3_{mon.} → P3_{hex.} → P'3_{mon.} → O3'_{hex.} → O3''_{hex.}). The intensity of the redox peaks of the Na[Ni_{0.5}Mn_{0.5}]O₂ cathode, especially during the hexagonal O3'–hexagonal O3'' phase transition, became gradually polarized and reduced in height with cycling, indicating high capacity fading continuously with structural degradation. In comparison, the redox peaks of the Na_{0.98}Ca_{0.01}[Ni_{0.5}Mn_{0.5}]O₂ cathode hardly changed, which is consistent with the excellent Na intercalation stability of the cathode. In addition, *ex situ* X-ray absorption near edge structure (XANES) analysis was conducted (Fig. 3a and S8†) to examine the oxidation state of transition metals during the charge–discharge process. For both cathodes in the as-prepared state, Ni and Mn were divalent (2+) and tetravalent (4+), respectively. The Ni K-edge absorption spectrum clearly shifted toward the higher energy region after charging at 4.3 V,

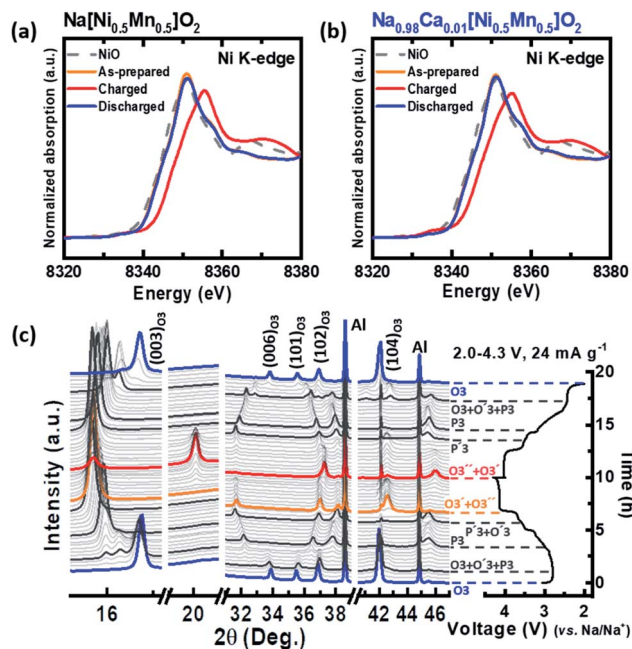


Fig. 3 *Ex situ* XANES spectra at the Ni-K absorption edge of (a) Na_{0.5}[Ni_{0.5}Mn_{0.5}]O₂ and (b) Na_{0.98}Ca_{0.01}[Ni_{0.5}Mn_{0.5}]O₂ cathodes with NiO as the reference oxide. (c) *Operando* XRD patterns and corresponding curves of Ca-substituted Na_{0.98}Ca_{0.01}[Ni_{0.5}Mn_{0.5}]O₂ cathode during the initial cycling of the material versus metallic sodium between 2 and 4.3 V at 24 mA g⁻¹.

indicating that a change in the oxidation state of nickel from the divalent state to the tetravalent state occurred due to electrochemical oxidation in the Na cell. In comparison, although a shape change of the white line was observed, which is associated with a local geometry change due to the redox reaction of the surrounding electrochemically active metals, no significant edge shift was observed at the Mn K-edge, suggesting that manganese ions are electrochemically inactive in the tetravalent state, which is consistent with other previous reports.^{12,28,29} On discharge, the average oxidation state of Ni returned to its original value. Furthermore, this reaction mechanism was also confirmed through prediction of the net magnetic moments on Mn and Ni ions of Na_x[Ni_{0.5}Mn_{0.5}]O₂ based on first-principles calculations. As presented in Fig. S9,† in the case of O3-Na₁[Ni_{0.5}Mn_{0.5}]O₂, the integrated spin moments of Ni and Mn atoms were approximately 0 and +3, respectively, which indicates the existence of Ni²⁺ and Mn⁴⁺ ions in O3-Na₁[Ni_{0.5}Mn_{0.5}]O₂. During 1 mol Na⁺ extraction from the structure, the integrated spin moment of the Mn atoms remained unaltered and that of the Ni atom gradually increased from 0 to +2, which indicates the Ni²⁺/Ni⁴⁺ redox reaction of O3-Na₁[Ni_{0.5}Mn_{0.5}]O₂ during Na ion extraction/insertion. This prediction is consistent with the experimental results based on the XANES analysis. These results suggest that 0.01 mol of Ca²⁺ ions was successfully incorporated into the Na layer rather than a transition metal layer without interrupting the charge-transfer reaction.

To gain insights into the role of Ca²⁺ ions in the crystal structure during the initial charge–discharge process, the structural evolution of Na_{0.98}Ca_{0.01}[Ni_{0.5}Mn_{0.5}]O₂ was

investigated *via operando* synchrotron XRD analysis, and the results are displayed in Fig. 3b. Upon charging (Na extraction), the (00 l) peaks of the hexagonal O3 phase (*i.e.* (003)_{hex.} and (006)_{hex.}) split into two and are shifted toward a lower angle, indicating a slightly enlarged interslab distance according to Bragg's equation ($2d \sin \theta = n\lambda$). On charging up to 4.0 V (extracting ≈ 0.65 mol of Na ions from the crystal structure), the Na_{0.98}Ca_{0.01}[Ni_{0.5}Mn_{0.5}]O₂ cathode experienced a typical phase transition of O3_{hex.} \rightarrow O'3_{mon.} \rightarrow P3_{hex.} \rightarrow P'3_{mon.}.^{11,13,19} In the voltage range of 2.8 to 3.5 V, the Na_{0.98}Ca_{0.01}[Ni_{0.5}Mn_{0.5}]O₂ cathode showed a tri-phase reaction with coexistence of the O3_{hex.}-O'3_{mon.}-P3_{hex.} phase compared to that of the Na[Ni_{0.5}Mn_{0.5}]O₂ cathode. Such a fast phase transition from O3 to the O3–P3 mixed phase in the early charging state could be attributed to the facile Na⁺ ion diffusion with smooth MeO₂ slab gliding and stabilization of the crystal structure because Na ions at prismatic sites become energetically stable when sodium ions are partly extracted from the O3-type phase.²³ When Na ions were further removed from the structure, simultaneously, a new O3 phase, indexed to O3'_{hex.} by Tarascon *et al.*, appeared and formed the major phase by the end of the plateau.^{16,22} Such a biphasic reaction at the end of the plateau has been typically observed in O3-type layered oxide materials when the Na ions are fully extracted from the structure.²⁷ Upon following the discharge process, the XRD pattern exhibited an opposite structural evolution, and the well-defined peaks corresponding to the O3 phase completely returned to the original positions at the discharge end, revealing a highly reversible O3–P3 phase transition of the Na_{0.98}Ca_{0.01}[Ni_{0.5}Mn_{0.5}]O₂ cathode. The *ex situ* XRD patterns at several charged states were also used to verify the structural reversibility during Na ion extraction/insertion. The XRD patterns were measured at the 2nd, 10th, and 20th cycles for both Na[Ni_{0.5}Mn_{0.5}]O₂ and Na_{0.98}Ca_{0.01}[Ni_{0.5}Mn_{0.5}]O₂ cathodes and are displayed in Fig. S10.† Compared to the Na[Ni_{0.5}Mn_{0.5}]O₂ cathode, the peak at $2\theta = 20.1^\circ$ was well maintained for the Na_{0.98}Ca_{0.01}[Ni_{0.5}Mn_{0.5}]O₂ cathode, which means that Ca²⁺ substitution allows the structure to fully extract Na⁺ ions repetitively. From these results, we hypothesize that Ca²⁺ ions on Na sites stabilize the structure when Na⁺ ions are almost fully extracted and lead to structural reversibility with improved cycle performances.

First-principles calculations

To investigate the electrochemical Na ion storage mechanism to predict the theoretical properties of Na_x[Ni_{0.5}Mn_{0.5}]O₂, we performed first-principles calculations based on the structural information verified through the Rietveld refinement analysis. At this stage, even though 0.01 mol of Ca²⁺ ions was incorporated into the bulk Na sites, Na_{0.98}Ca_{0.01}[Ni_{0.5}Mn_{0.5}]O₂ showed a nearly identical crystal structure with Na[Ni_{0.5}Mn_{0.5}]O₂; hence, we assumed that Na_{0.98}Ca_{0.01}[Ni_{0.5}Mn_{0.5}]O₂ experienced the same O3–P3 phase transformation during the Na⁺ extraction/insertion process. Various Na/vacancy configurations on O3-Na_x[Ni_{0.5}Mn_{0.5}]O₂ compositions ($0 \leq x \leq 1$) were generated through the cluster assisted statistical mechanics (CASM) code and then, we predicted the theoretical formation energies of the

O3-Na_x[Ni_{0.5}Mn_{0.5}]O₂ composition. Based on information of the formation energies, we calculated the redox potentials of O3-Na_x[Ni_{0.5}Mn_{0.5}]O₂ during Na⁺ extraction/insertion using the following equation

$$V = -\frac{E[\text{Na}_{x_2}[\text{Ni}_{0.5}\text{Mn}_{0.5}]\text{O}_2] - E[\text{Na}_{x_1}[\text{Ni}_{0.5}\text{Mn}_{0.5}]\text{O}_2] - (x_2 - x_1)E[\text{Na}]}{(x_2 - x_1)F} \quad (1)$$

where $E(x)$ indicates the formation energy on the most stable Na/vacancy configuration of x species. By considering the typical O3–P3 phase transition in the O3-type layered oxide cathode in SIBs, we calculated the formation energies of P3-Na_x[Ni_{0.5}Mn_{0.5}]O₂ and then applied this information to compare the thermodynamic stability between O3- and P3-phases. As presented in Fig. 4a, we predicted that the O3–P3 phase transition occurred after extraction of 0.25 mol of Na ions from O3-Na₁[Ni_{0.5}Mn_{0.5}]O₂, and then, when the Na content in P3-Na_x[Ni_{0.5}Mn_{0.5}]O₂ was reduced to less than 0.25 mol, the O3–P3 phase transition re-occurred. Moreover, we verified that in the case of O3/P3-Na_x[Ni_{0.5}Mn_{0.5}]O₂, the redox potentials required for Na⁺ extraction/insertion were less than ~4.11 V (vs. Na⁺/Na) and more than ~2.48 V, which indicates that 1 mol of Na ions can be reversibly extracted/inserted from/into the O3-Na₁[Ni_{0.5}Mn_{0.5}]O₂ structure despite the O3–P3 phase transition.

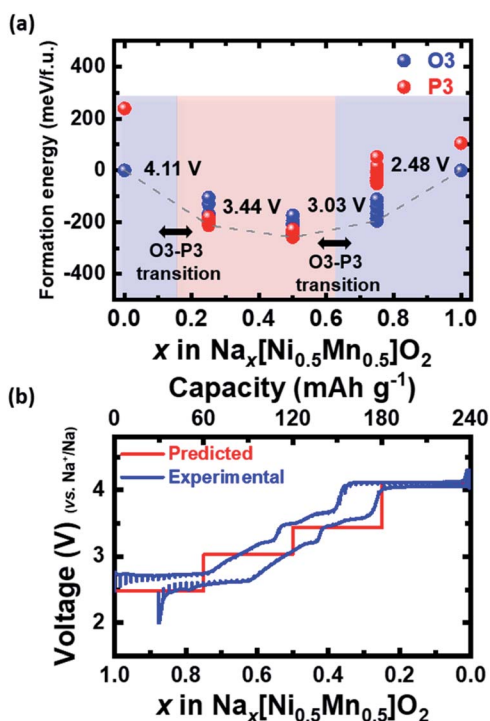


Fig. 4 (a) Convex-hull plot of formation energies of O3/P3-Na_x[Ni_{0.5}Mn_{0.5}]O₂ ($0 \leq x \leq 1$). (b) Theoretical redox potentials of O3/P3-Na_x[Ni_{0.5}Mn_{0.5}]O₂ ($0 \leq x \leq 1$) predicted by first-principles calculations and the experimentally measured GITT charge/discharge curve of Na_{0.98}Ca_{0.01}[Ni_{0.5}Mn_{0.5}]O₂ cathode.

Fig. 4b illustrates the predicted redox potential range of the O3/P3-Na_x[Ni_{0.5}Mn_{0.5}]O₂ cathode as a function of the Na content ($0 \leq x \leq 1$) with experimentally measured galvanostatic intermittent titration technique (GITT) profiles in the voltage range

of 2.0–4.3 V. To confirm our hypothesis that the Ca-substituted cathode would undergo a similar O3–P3 phase transformation during the sodiation/de-sodiation process, we checked the GITT profiles of the Na_{0.98}Ca_{0.01}[Ni_{0.5}Mn_{0.5}]O₂ cathode and overlaid the results with the predicted theoretical redox potential of the Na_x[Ni_{0.5}Mn_{0.5}]O₂ cathode. Interestingly, we confirmed that the slope of the charge/discharge curve of O3-Na_{0.98}Ca_{0.01}[Ni_{0.5}Mn_{0.5}]O₂ matched the predicted redox potential of the Na_x[Ni_{0.5}Mn_{0.5}]O₂ cathode well within the wide voltage window of 2.0–4.3 V; this clearly verified our hypothesis and confirmed that ~1.0 mol of Na⁺ ions could be extracted/inserted from/into Na_{0.98}Ca_{0.01}[Ni_{0.5}Mn_{0.5}]O₂.

Simultaneously, the predicted structural changes of O3-Na_x[Ni_{0.5}Mn_{0.5}]O₂ during Na⁺ extraction/insertion are presented in Fig. 5a. With extraction of 0.75 mol of Na from O3-Na₁[Ni_{0.5}Mn_{0.5}]O₂, the c -lattice parameter gradually increased from ~15.97 to ~17.40 Å because of the reinforced repulsive force between O²⁻ anions. Then, after an additional 0.25 mol Na extraction, it decreased to ~15.24 Å owing to MeO₂ slab gliding

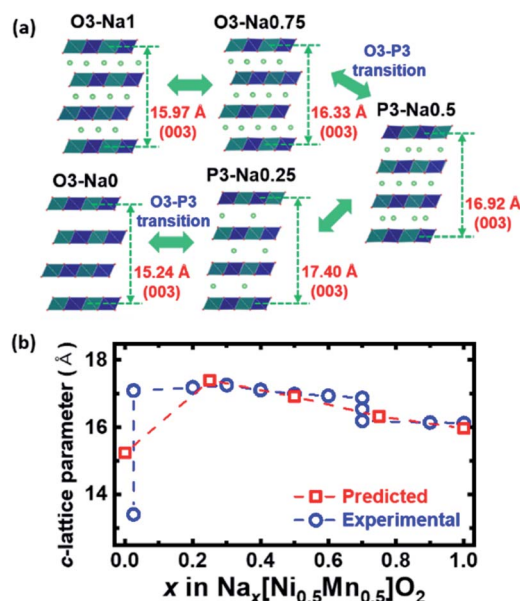


Fig. 5 (a) The predicted structural changes of O3/P3-Na_x[Ni_{0.5}Mn_{0.5}]O₂ ($0 \leq x \leq 1$) during Na⁺ extraction/insertion as a function of Na content. (b) Comparison of the lattice parameters of O3/P3-Na_x[Ni_{0.5}Mn_{0.5}]O₂ ($0 \leq x \leq 1$) predicted through first-principles calculations and O3/P3-Na_xCa_{0.01}[Ni_{0.5}Mn_{0.5}]O₂ verified through Rietveld refinement based on *operando* XRD analysis.

arising from the structural instability, which matched well with the structural change of other layered-type cathode materials for SIBs.^{16,22,30,31} Furthermore, as shown in Fig. 5b, we compared the *c*-lattice parameters of various O3-/P3-Na_xCa_{0.01}[Ni_{0.5}Mn_{0.5}]O₂ verified through Rietveld refinement based on *operando* XRD results and those of O3/P3-Na_x[Ni_{0.5}Mn_{0.5}]O₂ predicted through the first-principles calculations. We confirmed that despite the occurrence of a partial two-phase reaction, the *c*-lattice parameter was increased in general during extraction of Na ions from O3-Na₁[Ni_{0.5}Mn_{0.5}]O₂ to P3-Na_{0.25}[Ni_{0.5}Mn_{0.5}]O₂. In the case of Na₀[Ni_{0.5}Mn_{0.5}]O₂, although two phases were detected in the XRD patterns of Na_xCa_{0.01}[Ni_{0.5}Mn_{0.5}]O₂ from the *operando* XRD analysis, the average value of *c*-lattice parameters on the two phases was similar to the *c*-lattice parameter predicted through first-principles calculations. Moreover, this result implies that at the Na₀[Ni_{0.5}Mn_{0.5}]O₂ composition, coexistence of O3' and O3'' phases is more favorable than perfect phase transition to the O3'' phase, which agrees with the experimental results of previous research studies.^{16,22}

Thus, we hypothesized that the decrease in volume change by Ca-substitution during charge/discharge enables better electrochemical performances of Na_{1-2x}Ca_x[Ni_{0.5}Mn_{0.5}]O₂ (*x* ≈ 0.04) than those of O3-Na[Ni_{0.5}Mn_{0.5}]O₂. As presented in Fig. 6, it was predicted through first-principles calculations that the volume difference between O3-Na₀Ca_x[Ni_{0.5}Mn_{0.5}]O₂ and P3-Na_{0.25}Ca_x[Ni_{0.5}Mn_{0.5}]O₂ is ≈ 8.20%, while that between O3-Na₀[Ni_{0.5}Mn_{0.5}]O₂ and P3-Na_{0.25}[Ni_{0.5}Mn_{0.5}]O₂ is ≈ 13.24%. These predicted data match well with the experimental results on comparison of XRD patterns between fully charged Na_{0.98}Ca_{0.01}[Ni_{0.5}Mn_{0.5}]O₂ and O3-Na[Ni_{0.5}Mn_{0.5}]O₂ electrodes. Fig. S11† shows that after charging to 4.3 V (vs. Na⁺/Na), more P3–O3 phase transition with growth of a new peak at 2θ = 20.1° occurred at P3-Na_x[Ni_{0.5}Mn_{0.5}]O₂ than Na_xCa_{0.01}[Ni_{0.5}Mn_{0.5}]O₂, which indicates a larger volume change of P3-Na_x[Ni_{0.5}Mn_{0.5}]O₂ than Na_xCa_{0.01}[Ni_{0.5}Mn_{0.5}]O₂ during Na extraction/insertion.

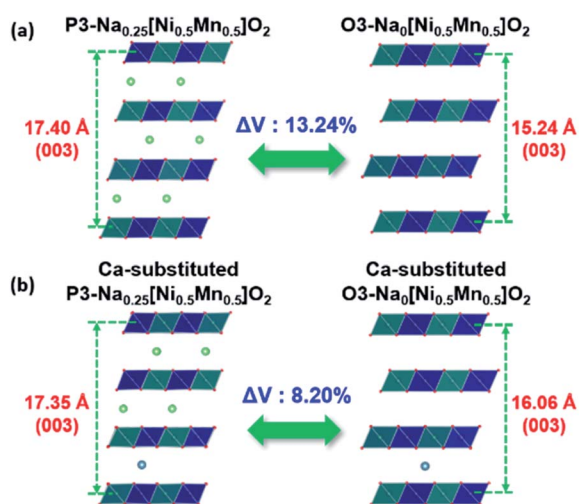


Fig. 6 (a) Comparison of the predicted crystal structure between O3-Na₀[Ni_{0.5}Mn_{0.5}]O₂ and P3-Na_{0.25}[Ni_{0.5}Mn_{0.5}]O₂. (b) Comparison of the predicted crystal structure between O3-Na₀Ca_{0.04}[Ni_{0.5}Mn_{0.5}]O₂ and P3-Na_{0.25}Ca_{0.04}[Ni_{0.5}Mn_{0.5}]O₂.

Because O3-Na[Ni_{0.5}Mn_{0.5}]O₂ experiences a severe structural change with O3'–O3'' phase transition during charging at high voltage (>4.0 V (vs. Na⁺/Na)), it is important to confirm suppression of structural change by Ca-substitution despite fully charging to 4.3 V. Thus, we performed Rietveld refinement on the XRD patterns of fully charged pristine Na[Ni_{0.5}Mn_{0.5}]O₂ and Na_{0.98}Ca_{0.01}[Ni_{0.5}Mn_{0.5}]O₂ electrodes. As presented in Fig. S12 and Table S4,† it was verified that the *c*-lattice parameters on the O3' and O3'' phases of fully charged pristine Na[Ni_{0.5}Mn_{0.5}]O₂ are 17.020 Å and 13.2919 Å, respectively, which are similar to those on O3' and O3'' phases of fully charged Na_{0.98}Ca_{0.01}[Ni_{0.5}Mn_{0.5}]O₂. The interesting point is the difference of O3'/O3'' ratio between fully charged pristine Na[Ni_{0.5}Mn_{0.5}]O₂ and Na_{0.98}Ca_{0.01}[Ni_{0.5}Mn_{0.5}]O₂ electrodes. While the proportions of O3' and O3'' phases in fully charged pristine Na[Ni_{0.5}Mn_{0.5}]O₂ are 12.24 and 87.75, respectively, those of O3' and O3'' phases in fully charged Na_{0.98}Ca_{0.01}[Ni_{0.5}Mn_{0.5}]O₂ are 19.48 and 80.52, respectively. Because transition to the O3'' phase is accompanied by a large decrease of *c*-lattice parameter on the layered-type structure, a smaller amount of O3'' phase in fully charged Na_{0.98}Ca_{0.01}[Ni_{0.5}Mn_{0.5}]O₂ than in fully charged Na[Ni_{0.5}Mn_{0.5}]O₂ indicates the suppressed structural change by Ca-substitution. These results agreed well with previous studies that the reduced volume change during Na extraction/insertion can result in enhanced electrochemical performances and structural stability of Na_x[Ni_{0.5}Mn_{0.5}]O₂.^{16,17,22} As a result, the XRD patterns of cycled Na[Ni_{0.5}Mn_{0.5}]O₂ displayed a Na-deficient phase such as monoclinic O'3 and hexagonal P3 in Fig. S13.† Although the original structure of Na[Ni_{0.5}Mn_{0.5}]O₂ was not found, Na_{0.98}Ca_{0.01}[Ni_{0.5}Mn_{0.5}]O₂ exhibited a nearly perfect O3-type structure. Furthermore, it is generally known that the Ca–O bond was stronger than the Na–O bond based on standard Gibbs energies of the formation of both oxides at 298 K;³² the decreased interlayer distance verified through Rietveld refinement analysis also confirms this stronger bonding (Na[Ni_{0.5}Mn_{0.5}]O₂: 3.12 Å; Na_{0.98}Ca_{0.01}[Ni_{0.5}Mn_{0.5}]O₂: 3.08 Å). Thus, we assumed that this is the reason for stabilization of the structure by Ca substitution on the O3-Na[Ni_{0.5}Mn_{0.5}]O₂. Moreover, from refinement data, we verified that in the formation of defects, the Ca²⁺ ion occupies the Na⁺ ion site to form a Ca at the Na site with a defect and a sodium vacancy.^{33,34} The defects in the material would increase the conductivity, improve the diffusion of sodium ions, and make the sodium ions easy to extract and insert into the material. This synergy by Ca²⁺ substitution enhanced the structural stability and improved the cycling performance not only over a wide voltage window but also in a narrow range of 2.0–4.0 V, as shown in Fig. S14.†

Toward practical sodium-ion batteries

Although tremendous efforts have resulted in the great advances in recent years, O3-type layered oxide cathode materials have been plagued by the issue of poor thermal stability and structural stability against a humid atmosphere, which are favorable properties for practical application. To confirm the practical acceptability, we first checked the thermal stability and air-stability of the Na_{0.98}Ca_{0.01}[Ni_{0.5}Mn_{0.5}]O₂ cathode by

comparing it with the $\text{Na}[\text{Ni}_{0.5}\text{Mn}_{0.5}]\text{O}_2$ cathode. Differential scanning calorimetry (DSC) was performed to observe the exothermic reactions of the deeply de-sodiated electrodes (highly unstable state) collected from cells charged to 4.3 V (vs. Na/Na^+) after the first cycle. The results are plotted in Fig. S15,† showing both onset temperature of the exothermic reactions and the total specific heat generation. Although a similar amount of Na^+ ions (according to charge capacities) was extracted from the crystal structure, the thermal reaction between $\text{Na}_x\text{Ca}_{0.01}[\text{Ni}_{0.5}\text{Mn}_{0.5}]\text{O}_2$ and $\text{Na}_x[\text{Ni}_{0.5}\text{Mn}_{0.5}]\text{O}_2$ (x is close to 0) cathodes was different. In contrast, the $\text{Na}_x[\text{Ni}_{0.5}\text{Mn}_{0.5}]\text{O}_2$ electrode displayed an exothermic peak at 254.1 °C with a heat generation of 634.5 J g^{-1} , the $\text{Na}_x\text{Ca}_{0.01}[\text{Ni}_{0.5}\text{Mn}_{0.5}]\text{O}_2$ electrode showed a lower heat generation of 352 J g^{-1} and an exothermic peak at 258.9 °C. It should be noted that the thermal reaction is related to the evolution of oxygen from the crystal structure because the oxygen released from the cathode materials can react with the electrolyte solution and undergo a redox reaction. Therefore, it is strongly believed that the improved thermal stability of the Ca-substituted cathode likely resulted from the strong interaction of immobile Ca^{2+} with O^{2-} , which suppresses the rate of release of thermal oxygen from the highly oxidized cathode material.

Another critical property of an electrode material toward practical application is the ease of handling against a moist environment.¹⁰ Most of the O3-type transition metal oxide cathodes reported so far are moisture sensitive because of the low redox potential associated with 3d-metals. Once the cathode is exposed to air or moisture, water oxidizes the transition metal ions with the concomitant removal of Na^+ ions, which further react with CO_2 and H_2O in air to form Na_2CO_3 or NaOH .²² Such undesirable reactions usually cause structural degradation and poor electrochemical performances and thus make them difficult to handle. As revealed in Fig. 7, after exposure to air with a relative humidity of $\approx 55\%$, the $\text{Na}[\text{Ni}_{0.5}\text{Mn}_{0.5}]\text{O}_2$ exhibited an apparent structural change to a Na-deficient monoclinic O'3 phase together with formation of $\text{Na}_2\text{CO}_3 \cdot n\text{H}_2\text{O}$ on the surface.²¹ In contrast,

$\text{Na}_{0.98}\text{Ca}_{0.01}[\text{Ni}_{0.5}\text{Mn}_{0.5}]\text{O}_2$ remarkably retarded spontaneous phase transition and retained the original O3 structure. To confirm in detail the structural stability against a humid atmosphere, a comparative study of the XRD evolution of the $\text{Na}_{0.98}\text{Ca}_{0.01}[\text{Ni}_{0.5}\text{Mn}_{0.5}]\text{O}_2$ and $\text{Na}[\text{Ni}_{0.5}\text{Mn}_{0.5}]\text{O}_2$ cathodes was conducted as a function of exposure time (1, 3, and 5 days and 1 week) (Fig. S16†). After 1 day, there were no significant structural changes in either cathode. However, after three days, the $\text{Na}[\text{Ni}_{0.5}\text{Mn}_{0.5}]\text{O}_2$ cathode was readily oxidized in the presence of moisture, and subsequently, the intensity of $(003)_{\text{hex}}$ and $(104)_{\text{hex}}$ peaks decreased in the XRD patterns. After 5 days, splitting of the $(003)_{\text{hex}}$ and $(006)_{\text{hex}}$ diffraction lines was observed, indicating a slightly enlarged interslab distance for the new monoclinic O3 phase. Finally, after 1 week, the phase transformation from the hexagonal O3 to the monoclinic O'3 phase occurred in the $\text{Na}[\text{Ni}_{0.5}\text{Mn}_{0.5}]\text{O}_2$ cathode. This monoclinic O'3 phase transformation can be observed in the sodium deficient structure when the sodium ions are extracted down to 20 mol% in the original O3 structure.^{10,20} In contrast, throughout the week, the intensified peaks, $(003)_{\text{hex}}$, $(006)_{\text{hex}}$, $(101)_{\text{hex}}$, $(102)_{\text{hex}}$, and $(104)_{\text{hex}}$, in the O3 phase were well retained persistently for the $\text{Na}_{0.98}\text{Ca}_{0.01}[\text{Ni}_{0.5}\text{Mn}_{0.5}]\text{O}_2$ cathode, indicating less reactivity against moisture. These results suggest that the Ca^{2+} ions on the Na sites with strong Ca–O bonding prevent the removal of Na^+ ions from the structure when exposed to air. As expected, in Fig. S17,† the $\text{Na}_{0.98}\text{Ca}_{0.01}[\text{Ni}_{0.5}\text{Mn}_{0.5}]\text{O}_2$ cathode demonstrated higher reversible capacity with lower voltage polarization and better cycling stability after prolonged exposure, while the $\text{Na}[\text{Ni}_{0.5}\text{Mn}_{0.5}]\text{O}_2$ cathode showed poor electrochemical performance and even exhibited an irreversible reaction during charging, due to the decomposition of Na_2CO_3 which is a by-

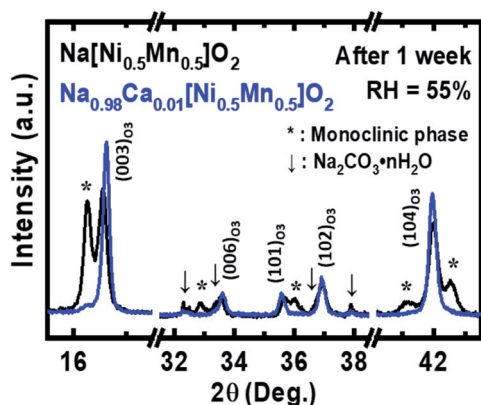


Fig. 7 Comparison of XRD patterns collected from $\text{Na}[\text{Ni}_{0.5}\text{Mn}_{0.5}]\text{O}_2$ and $\text{Na}_{0.98}\text{Ca}_{0.01}[\text{Ni}_{0.5}\text{Mn}_{0.5}]\text{O}_2$ cathodes after 1 week of exposure to air with a relative humidity (RH) of $\approx 55\%$. The $\text{Na}[\text{Ni}_{0.5}\text{Mn}_{0.5}]\text{O}_2$ gradually transformed into a monoclinic phase, while $\text{Na}_{0.98}\text{Ca}_{0.01}[\text{Ni}_{0.5}\text{Mn}_{0.5}]\text{O}_2$ retained its initial O3 structure very well.

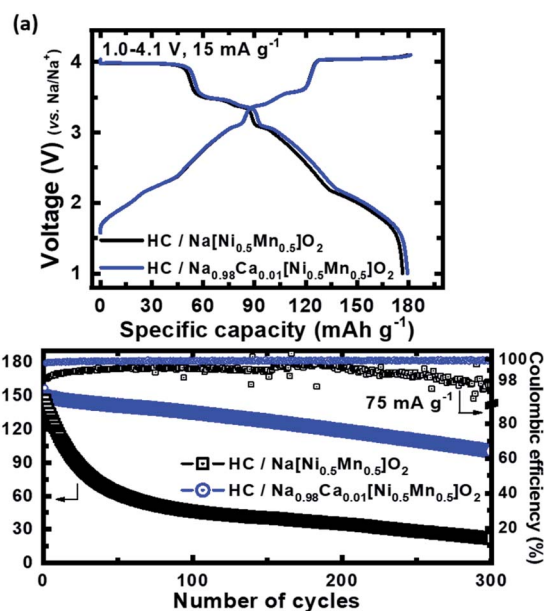


Fig. 8 Electrochemical performances of the prototype pouch full cell using $\text{Na}[\text{Ni}_{0.5}\text{Mn}_{0.5}]\text{O}_2$ and $\text{Na}_{0.98}\text{Ca}_{0.01}[\text{Ni}_{0.5}\text{Mn}_{0.5}]\text{O}_2$ cathodes with a hard carbon (HC) anode: (a) typical voltage profiles of initial charge–discharge between 1.0 and 4.1 V at 15 mA g^{-1} at 25°C and (b) long-term cycling stability test at 75 mA g^{-1} at 30°C .

product of removed Na^+ ions and CO_2 in air.^{22,35} Such a comparison of the thermal properties and air-stability strengthens the merits of Ca-substituted cathodes in practical application.

In an attempt to highlight the practical applicability of the proposed $\text{Na}_{0.98}\text{Ca}_{0.01}[\text{Ni}_{0.5}\text{Mn}_{0.5}]\text{O}_2$ cathode, finally, we fabricated and examined a prototype pouch full cell using a relatively high active mass loading cathode (approximately 10 mg cm^{-2}) with a hard carbon anode. The assembled pouch full cells were tested at 15 mA g^{-1} in the voltage range of 1.0–4.1 V after a degassing process during the first cycle. In Fig. 8a, the prototype pouch full cell of both $\text{Na}[\text{Ni}_{0.5}\text{Mn}_{0.5}]\text{O}_2$ and $\text{Na}_{0.98}\text{Ca}_{0.01}[\text{Ni}_{0.5}\text{Mn}_{0.5}]\text{O}_2$ delivered a reversible capacity of $\approx 180 \text{ mA h g}^{-1}$ with an average operating potential of 3.1 V. As expected, the $\text{HC}/\text{Na}_{0.98}\text{Ca}_{0.01}[\text{Ni}_{0.5}\text{Mn}_{0.5}]\text{O}_2$ full cell exhibited excellent cycling stability with a capacity retention of 67% over 300 cycles compared to $\text{HC}/\text{Na}[\text{Ni}_{0.5}\text{Mn}_{0.5}]\text{O}_2$ which experienced a drastic capacity fading with lower efficiency incurred by irreversible phase transition (Fig. 8b). After 50 cycles, the $\text{HC}/\text{Na}[\text{Ni}_{0.5}\text{Mn}_{0.5}]\text{O}_2$ retained only 25% of the initial capacity because the cell was already impaired, which led to an irregular fluctuation of coulombic efficiency.

Conclusions

In summary, we have shown that Ca substitution into bulk Na sites can significantly improve the structural and electrochemical properties of the $\text{Na}[\text{Ni}_{0.5}\text{Mn}_{0.5}]\text{O}_2$ cathode. A combination of experimental and theoretical studies was conducted to verify the details of the sodium storage mechanism and superiority of the proposed $\text{Na}_{0.98}\text{Ca}_{0.01}[\text{Ni}_{0.5}\text{Mn}_{0.5}]\text{O}_2$ cathode. Because of the strong interaction between Ca^{2+} and O^{2-} , the presence of Ca^{2+} ions in Na sites sufficiently stabilized the crystal structure and effectively mitigated the volume expansion when extracting maximum Na ions from $\text{Na}_{0.98}\text{Ca}_{0.01}[\text{Ni}_{0.5}\text{Mn}_{0.5}]\text{O}_2$. As a result, $\text{Na}_{0.98}\text{Ca}_{0.01}[\text{Ni}_{0.5}\text{Mn}_{0.5}]\text{O}_2$ delivered a high initial capacity of 209 mA h g^{-1} with a better cycling stability and 75% capacity retention after 100 cycles in a wide voltage window of 2.0–4.3 V. Furthermore, Ca-substitution significantly improved the practical applicability with high thermal stability and structural stability against moisture. Especially, the scaled-up prototype pouch full cell exhibited an excellent capacity retention of 67% over 300 cycle. Although the Ca-substitution can suppress the structural change of $\text{O}3\text{-Na}_x[\text{Ni}_{0.5}\text{Mn}_{0.5}]\text{O}_2$ at the fully charged state, the $\text{O}3'\text{-O}3''$ phase transition does not perfectly disappear. Thus, attempts need to be made to further improve the retention of the O3-based crystal structure of $\text{Na}_x[\text{Ni}_{0.5}\text{Mn}_{0.5}]\text{O}_2$, eliminating the destructive phase transitions. We believe that our novel approach could be applicable to many other layered oxide materials and could facilitate the development of advanced and practical SIBs with high energy density.

Experimental

Synthesis of materials

Spherical $[\text{Ni}_{0.5}\text{Mn}_{0.5}](\text{OH})_2$ precursors were synthesized by the co-precipitation method.¹⁹ Stoichiometric amounts of $\text{NiSO}_4 \cdot 6\text{H}_2\text{O}$ and $\text{MnSO}_4 \cdot \text{H}_2\text{O}$ (Samchun Chemical, Korea) were used

as starting materials for $[\text{Ni}_{0.5}\text{Mn}_{0.5}](\text{OH})_2$. The metal solution concentration (2 mol L^{-1} for the metal solution), pH (~ 11.0), temperature ($45 \text{ }^\circ\text{C}$), and stirring speed of the mixture in the batch-type reactor were carefully controlled. At the same time, aqueous NaOH (Samchun, Korea; NaOH/transition metal molar ratio = 2 : 1) and aqueous NH_4OH (Junsei, Japan; NH_4OH /transition metal molar ratio = 1.1 : 1) as chelating agents were separately fed into the reactor. The precursor powders were obtained by filtering, washing and vacuum drying at $110 \text{ }^\circ\text{C}$ overnight. For the $\text{Na}[\text{Ni}_{0.5}\text{Mn}_{0.5}]\text{O}_2$ cathode, the obtained spherical precursors were mixed with Na_2CO_3 (Na : [Ni + Mn] molar ratio = 1.05 : 1, 5% excess Na_2CO_3), calcined at $800 \text{ }^\circ\text{C}$ for 24 h in an oxygen atmosphere, and quenched under vacuum conditions. For Ca-substituted $\text{Na}_{1-2x}\text{Ca}_x[\text{Ni}_{0.5}\text{Mn}_{0.5}]\text{O}_2$ cathodes, an appropriate amount of $\text{Ca}(\text{OH})_2$ was mixed with the $[\text{Ni}_{0.5}\text{Mn}_{0.5}](\text{OH})_2$ precursor and Na_2CO_3 (Na : Ca : [Ni + Mn] molar ratio = 1.05–2x : x : 1, x = 0.01, 0.02, and 0.03) in the same calcination process.

Materials characterization

The morphologies of the prepared powders were observed using scanning electron microscopy (SEM, Verios G4UC, JEOL). Transmission electron microscopy (TEM, JEM2010, JEOL) and energy dispersive X-ray spectroscopy (EDX, JEM 2100F, JEOL) were carried out. To characterize the crystal structures of the synthesized powders, high-resolution synchrotron powder X-ray diffraction (SPXRD) was carried out at the 9B-HRPD beamline of the Pohang Accelerator Laboratory (PAL), Pohang, Korea. SPXRD data were collected at a wavelength of 1.5225 \AA in the 2θ range of 10° to 130° , with a step size of 0.01° . The *operando* synchrotron XRD experiments were performed at the 6D beamline of PAL. The wavelength ($\lambda = 0.65303 \text{ \AA}$) of the incident beam and the sample detector distance were calibrated using an LaB_6 standard. A modified 2032 coin-type half-cell with a 3 mm diameter hole at its center containing a Kapton window served as the X-ray beam path. While the cell was being charged by applying a constant current of 24 mA g^{-1} , the XRD patterns were continuously recorded using a 2D charge-coupled device detector (MX225-HS, Rayonix) in transmission mode. The *ex situ* XAS measurements were carried out at the 1D beamline of PAL. Absorption energy level calibration was performed with metal foil as the reference. *Ex situ* XRD experiments for characterization of several electrodes (Empyrean, Panalytical) were conducted using Cu $K\alpha$ radiation in the reflection mode. XRD patterns were obtained in the 2θ range of 10 to 80° with a step size of 0.03° . To avoid exposure to air or moisture, we used a special XRD sample folder with a Mylar film.

Electrochemical tests

Electrochemical testing was performed in a 2032 coin-type cell using Na metal (Sigma Aldrich, USA) as the anode. Electrodes were fabricated by blending the prepared cathode powders (85 wt%), carbon black (10 wt%), and polyvinylidene fluoride (5 wt%) in *N*-methyl-2-pyrrolidone (Daejung Chem, Korea). The slurry was then cast on aluminum foil (Hohsen Corp., Japan) and pre-dried at $110 \text{ }^\circ\text{C}$ in an oven. Then, the electrode was

further dried at 110 °C for 5 h in a vacuum oven, and the disks were punched out of the foil. The electrolyte solution was 0.5 M NaPF₆ (Tokyo Chemical Industry, Japan) in a 1 : 1 volumetric mixture of ethylene carbonate (Sigma Aldrich, USA) and diethyl carbonate (Sigma Aldrich, USA) with 2 vol% fluoroethylene carbonate (Tokyo Chemical Industry, Japan). All cells were prepared in an Ar-filled glovebox (MBRAUN, Germany). The fabricated cathodes and sodium metal anodes were separated by a glass fiber (Advantec, USA) to prevent short circuiting. The loading amount of the active material for all electrodes was 3.0–4.0 mg cm⁻² in the coin-type half-cell. The cells were typically tested in the constant current mode, within the voltage range of 2.0–4.3 V *versus* Na/Na⁺, where 1C = 150 mA g⁻¹. For the full-cell test, pouch-type (3 × 5 cm) cells were fabricated and tested in the voltage range of 1.0–4.1 V at 15 mA g⁻¹ at 25 °C. The loading amount of the active material was 9.5–10.0 mg cm⁻². The anode was fabricated by blending hard carbon (provided by Aekyung Petrochemical, Korea) (80 wt%), carbon black (3 wt%), and polyvinylidene fluoride (17 wt%). The resulting slurry was covered over copper foil and dried at 110 °C for 5 h in a vacuum oven. The full cell balance was achieved by controlling the capacity ratio of anode to cathode (*N/P* ratio) at 1.15 : 1.^{19,36,37}

Computational details

Density functional theory (DFT) calculations were performed using the Vienna *ab initio* simulation package (VASP).³⁸ Projector-augmented wave (PAW) pseudopotentials were used with a plane-wave basis set,³⁹ as implemented in VASP. The Perdew–Burke–Ernzerhof (PBE) parametrization of the generalized gradient approximation (GGA) was used for the exchange–correlation functional.⁴⁰ The GGA+U method⁴¹ was adopted to address the localization of d-orbitals in Ni (*U* = 6.0 eV) and Mn (*U* = 3.9 eV), which is consistent with the previous report.⁴² All calculations were performed with an energy cutoff of 500 eV until the residual forces in the system converged to less than 0.03 eV Å⁻¹ per unit cell. Cluster-assisted statistical mechanics (CASM) software was used for the generation of all Na/vacancy configurations for each composition; this was followed by full DFT calculations on a maximum of 40 configurations with the lowest electrostatic energy for each composition.⁴³

Thermal properties of the de-sodiated cathodes

For DSC analysis, 2032 coin-type cells were charged to 4.3 V and opened in an Ar-filled dry box. After the remaining electrolyte solution was carefully removed from the surface of the electrode with dimethyl carbonate, the cathode materials were scraped from the current collector and packed in a stainless-steel container with a gold-plated copper pan. Measurements were performed using 7 mg of active materials with 100 μL fresh electrolyte solution using a DSC 214 Polyma (Netzsch, Germany) at a temperature scan rate of 5 °C min⁻¹.

Air stability tests

For the tests under controlled humidity, saturated Mg(NO₃)₂ salt solution was stored below the samples in a closed desiccator at 25 °C to maintain the relative humidity. The relative

humidity of saturated Mg(NO₃)₂ salt solution at 25 °C is ≈ 55%.⁴⁴ The exposed samples were also tested in half cells following the mentioned process after 1 week of exposure.

Conflicts of interest

There are no conflicts to declare.

Acknowledgements

This study was mainly supported by the Human Resources Development program (No. 20184010201720) of a Korea Institute of Energy Technology Evaluation and Planning (KETEP) grant funded by the Ministry of Trade, Industry and Energy of the Korean government. And this study was also supported by a National Research Foundation of Korea (NRF) grant funded by the Korea government Ministry of Education, Science and Technology (MEST) (NRF-2018R1A2B3008794).

References

- 1 B. Scrosati, J. Hassoun and Y.-K. Sun, *Energy Environ. Sci.*, 2011, **4**, 3287.
- 2 K. Turcheniuk, D. Bondarev, V. Singhal and G. Yushin, *Nature*, 2018, **559**, 467.
- 3 H. H. Sun, H.-H. Ryu, U.-H. Kim, J. A. Weeks, A. Heller, Y.-K. Sun and C. B. Mullins, *ACS Energy Lett.*, 2020, **5**, 1136.
- 4 J.-Y. Hwang, S.-T. Myung and Y.-K. Sun, *Chem. Soc. Rev.*, 2017, **46**, 3529.
- 5 K. Kubota, S. Kumakura, Y. Yoda, K. Kuroki and S. Komaba, *Adv. Energy Mater.*, 2018, **8**, 1703415.
- 6 J. Deng, W.-B. Luo, S.-L. Chou, H.-K. Liu and S.-X. Dou, *Adv. Energy Mater.*, 2017, **8**, 1701428.
- 7 N. Yabuuchi, H. Yoshida and S. Komaba, *Electrochemistry*, 2012, **80**, 716.
- 8 K. Kubota, I. Ikeuchi, T. Nakayama, C. Takei, N. Yabuuchi, H. Shiiba, M. Nakayama and S. Komaba, *J. Phys. Chem. C*, 2015, **119**, 166.
- 9 J.-Y. Hwang, C. S. Yoon, I. Belharouak and Y.-K. Sun, *J. Mater. Chem. A*, 2016, **4**, 17952.
- 10 P.-F. Wang, Y. You, Y.-X. Yin and Y.-G. Guo, *Adv. Energy Mater.*, 2018, **8**, 1701912.
- 11 S. Komaba, N. Yabuuchi, T. Nakayama, A. Ogata, T. Ishikawa and I. Nakai, *Inorg. Chem.*, 2012, **51**, 6211.
- 12 X. Xia and J. R. Dahn, *J. Electrochem. Soc.*, 2012, **159**, A1048.
- 13 P.-F. Wang, Y. You, Y.-X. Yin and Y.-G. Guo, *J. Mater. Chem. A*, 2016, **4**, 17660.
- 14 E. d. l. Llave, V. Borgel, K.-J. Park, J.-Y. Hwang, Y.-K. Sun, P. Hartmann, F.-F. Chesneau and D. Aurbach, *ACS Appl. Mater. Interfaces*, 2016, **8**, 1867.
- 15 S.-M. Oh, S.-T. Myung, M.-W. Jang, B. Scrosati, J. Hassoun and Y.-K. Sun, *Phys. Chem. Chem. Phys.*, 2013, **15**, 3827.
- 16 S. Mariyappan, Q. Wang and J. M. Tarascon, *J. Electrochem. Soc.*, 2018, **165**, A3714.
- 17 D. D. Yuan, Y. X. Wang, Y. L. Cao, X. P. Ai and H. X. Yang, *ACS Appl. Mater. Interfaces*, 2015, **7**, 8585.

- 18 P.-F. Wang, H.-R. Yao, X.-Y. Liu, J.-N. Zhang, L. Gu, X.-Q. Yu, Y.-X. Yin and Y.-G. Guo, *Adv. Mater.*, 2017, **29**, 1700210.
- 19 J.-Y. Hwang, T.-Y. Yu and Y.-K. Sun, *J. Mater. Chem. A*, 2018, **6**, 16854.
- 20 M. Sathiya, Q. Jacquet, M.-L. Doublet, O. M. Karakulina, J. Hadermann and J.-M. Tarascon, *Adv. Energy Mater.*, 2018, **8**, 1702599.
- 21 H.-R. Yao, P.-F. Wang, Y. Gong, J. Zhang, X. Yu, L. Gu, C. OuYang, Y.-X. Yin, E. Hu, X.-Q. Yang, E. Stavitski, Y.-G. Guo and L.-J. Wan, *J. Am. Chem. Soc.*, 2017, **139**, 8440.
- 22 Q. Wang, S. Mariyappan, J. Vergnet, A. M. Abakumov, G. Rousse, F. Rabuel, M. Chakir and J.-M. Tarascon, *Adv. Energy Mater.*, 2019, **26**, 1901785.
- 23 L. Sun, Y. Xie, X.-Z. Liao, H. Wang, G. Tan, Z. Chen, Y. Ren, J. Gim, W. Tang, Y.-S. He, K. Amine and Z.-F. Ma, *Small*, 2018, **14**, 1704523.
- 24 L. Zheng, J. C. Bennett and M. N. Obrovac, *J. Electrochem. Soc.*, 2019, **166**, A2058.
- 25 R. D. Shannon, *Acta Crystallogr., Sect. A: Cryst. Phys., Diffr., Theor. Gen. Crystallogr.*, 1976, **32**, 751.
- 26 M. D. Radin and A. Van der Ven, *Chem. Mater.*, 2016, **28**, 7898.
- 27 J. Vinckevičiūtė, M. D. Radin and A. Van der Ven, *Chem. Mater.*, 2016, **28**, 8640.
- 28 W.-S. Yoon, C. P. Grey, M. Balasubramanian, X.-Q. Yang and J. McBreen, *Chem. Mater.*, 2003, **15**, 3161.
- 29 M. Jeong, H. Lee, J. Yoon and W.-S. Yoon, *J. Power Sources*, 2019, **439**, 227064.
- 30 Y.-N. Zhou, P.-F. Wang, X.-D. Zhang, L.-B. Huang, W.-P. Wang, Y.-X. Yin, S. Xu and Y.-G. Guo, *ACS Appl. Mater. Interfaces*, 2019, **11**(27), 24184.
- 31 B. M. d. Boisse, J. H. Cheng, D. Carlier, M. Guignard, C. J. Pan, S. Bordere, D. Filimonov, C. Drathen, E. Suard, B. J. Hwang, A. Wattiaux and C. Delmas, *J. Mater. Chem. A*, 2015, **3**, 10976.
- 32 D. R. Lide, *Handbook of Chemistry and Physics*, CRC Press, London, 76th edn, 1995.
- 33 N. Kuganathan, N. Kelaidis and A. Chroneos, *Materials*, 2019, **12**, 3243.
- 34 N. Kuganathan and A. Chroneos, *Materials*, 2019, **12**, 1348.
- 35 M. Sathiya, J. Thomas, D. Batuk, V. Pimenta, R. Gopalan and J.-M. Tarascon, *Chem. Mater.*, 2017, **29**, 5948.
- 36 J.-Y. Hwang, S.-T. Myung, J. U. Choi, C. S. Yoon, H. Yashiro and Y.-K. Sun, *J. Mater. Chem. A*, 2017, **5**, 23671.
- 37 T.-Y. Yu, J.-Y. Hwang, I. T. Bae, H.-G. Jung and Y.-K. Sun, *J. Power Sources*, 2019, **422**, 1.
- 38 G. Kresse and J. Furthmüller, *Comput. Mater. Sci.*, 1996, **6**, 15.
- 39 P. E. Blöchl, *Phys. Rev. B: Condens. Matter Mater. Phys.*, 1994, **50**, 17953.
- 40 J. P. Perdew, K. Burke and M. Ernzerhof, *Phys. Rev. Lett.*, 1996, **77**, 3865.
- 41 V. I. Anisimov, F. Aryasetiawan and A. I. Lichtenstein, *J. Phys.: Condens. Matter*, 1997, **9**, 767.
- 42 A. Jain, G. Hautier, S. P. Ong, C. J. Moore, C. C. Fischer, K. A. Persson and G. Ceder, *Phys. Rev. B: Condens. Matter Mater. Phys.*, 2011, **84**, 045115.
- 43 A. Van der Ven, J. C. Thomas, Q. Xu and J. Bhattacharya, *Math. Comput. Simul.*, 2010, **80**, 1393.
- 44 L. Zhang, J.-M. Tarascon, M. T. Sougrati, G. Rousse and G. Chen, *J. Mater. Chem. A*, 2015, **3**, 16988.